NJC

Accepted Manuscript

This is an *Accepted Manuscript*, which has been through the Royal Society of Chemistry peer review process and has been accepted for publication.

Accepted Manuscripts are published online shortly after acceptance, before technical editing, formatting and proof reading. Using this free service, authors can make their results available to the community, in citable form, before we publish the edited article. We will replace this *Accepted Manuscript* with the edited and formatted *Advance Article* as soon as it is available.

You can find more information about *Accepted Manuscripts* in the Information for Authors.

Please note that technical editing may introduce minor changes to the text and/or graphics, which may alter content. The journal's standard Terms & Conditions and the Ethical guidelines still apply. In no event shall the Royal Society of Chemistry be held responsible for any errors or omissions in this *Accepted Manuscript* or any consequences arising from the use of any information it contains.

ROYAL SOCIETY OF CHEMISTRY

www.rsc.org/njc

Magnetically recoverable Fe_3O_4-implanted Ag-loaded ZnO nanoflakes for bacteria-inactivation and photocatalytic degradation of organic pollutants

Chockalingam Karunakaran* and Pazhamalai Vinayagamoorthy

Department of Chemistry, Annamalai University, Annamalainagar 608002, Tamilnadu, India

Corresponding author:

Professor Dr. C. Karunakaran
CSIR Emeritus Scientist
Department of Chemistry
Annamalai University
Annamalainagar 608002
Tamilnadu
India
E-mail: karunakaranc@rediffmail.com
Tel: +919443481590

Abstract

Fe_3O_4-Implanted Ag-loaded (0.3 % at.) perforated ZnO nanoflakes have been synthesized by a two-step method. Scanning electron and high resolution transmission electron micrographs (HRTEM) display the morphology and the energy dispersive X-ray spectrum confirms the presence of the constituent elements. HRTEM reveals the core/shell structure and Ag-deposition. Selected area electron diffraction pattern displays the presence of Fe_3O_4, ZnO and metallic Ag. The X-ray diffractogram and Raman spectrum are characteristic of Ag-deposited ZnO lattice. The M-H loop confirms the presence of magnetic core and the charge transfer resistance of the composite is less than that of pristine ZnO. The nanoflakes display moderate visible light absorption. The UV absorption and the emission spectrum of the composite are similar to those of pristine ZnO. The decay of photogenerated charge carriers in the nanocomposite is not significantly different from that in pristine ZnO. The composite nanoflakes are magnetically recoverable and inactivate bacteria such as *E. coli* in absence of illumination and photocatalytically degrade dye such as methylene blue effectively. Thus the synthesized composite nanoflakes address (i) bacteria disinfection, (ii) mineralization of organic pollutants and (iii) magnetic recovery of nanomaterial.

Keywords: core/shell nanosheets, photocatalyst, bacteria disinfection, semiconductor

1. Introduction

Population explosion and large economic growth in developing countries lead to mushrooming of chemical and manufacturing industries which results in highly polluted surface water and air. Water is a basic essential requirement of all the living beings and bacterial contamination of surface water is prevalent in tropical countries. Providing safe and portable water requires removal of pollutants and disinfection of bacteria. Hence a safe, cheap, easily handled and portable technique which does not consume any chemical is the need of the hour. Semiconductor-photocatalyzed mineralization of organic pollutants is an emerging technique. Now ceramic nanomaterials find use as bactericide as they are safe and easy to handle. ZnO is stable at pH 4-9 and is a promising photocatalytic material.[1] Loading of metallic Ag on ZnO nanocrystals is widely known to enhance the photocatalytic activity.[2-6] In addition, loading of Ag on ZnO by deposition method is reported to provide superior photocatalytic activity than that by coprecipitation or solvothermal technique.[7] Nanocrystalline ZnO is also an ecofriendly bactericide;[8] Zn^{2+} ion is a micronutrient for plants. The antibacterial activity of metallic silver, especially at nanosize, is well known.[9] Enhancement of the antibacterial activity of nanocrystalline ZnO on deposition of metallic Ag has been well established and the synthesized nanocomposite is more effective in inactivation of bacteria than the individual components.[10] Karunakaran et al., have reported that the bactericidal activity of Ag-deposited nanocrystalline ZnO obtained by photodeposition[11] or sol-gel technique[12] or microwave synthesis[13] or combustion method[14] is larger than that of the corresponding pristine ZnO. Hence Ag-loaded ZnO nanomaterial could be an effective photocatalyst cum bactericide. Recovery of the photocatalyst

nanoparticles from the treated effluent is the stumbling block for the use of nanocrystals for water purification. A possible solution is magnetic separation.[15] Zinc oxide-iron oxide composites do not serve the purpose as the latter is susceptible to corrosion.[16] Implantation of a superparamagnetic Fe_3O_4 core in silver-deposited ZnO nanomaterial is to make possible magnetic recovery of the photocatalyst without compromising the photocatalytic and bactericidal properties of Ag-loaded ZnO. This is the first report of synthesis of magnetically recoverable antibacterial photocatalytic nanoflakes for water treatment; the synthesized nanocomposite with Fe_3O_4 as core and ZnO deposited with metallic Ag as shell is recoverable with a tiny magnet and the Ag-loaded core/shell nanoflakes inactivate bacteria such as *E. coli* without any illumination and degrade dyes such as methylene blue under UV-A light.

2. Experimental

2.1. Synthesis of Fe_3O_4/Ag-ZnO nanoflakes

Fe_3O_4-Implanted Ag-deposited ZnO nanoflakes were obtained by a two-step synthesis. First, Fe_3O_4-implanted ZnO nanoflakes were synthesized by hydrothermal method. Fe_3O_4 nanocrystals (25 mg, Sigma-Aldrich) were dispersed in deionized distilled water (10 mL) under sonication. To the dispersion was added 10 mL of an aqueous solution containing 2 g of poly(ethylene glycol) 20000 under stirring. This was followed by drop wise addition of 10 mL of 0.5 M zinc acetate solution, also under stirring. To the resulting dispersion was added polyvinylpyrrolidone (0.5 g) followed by 1 M urea solution (10 mL) drop wise with stirring. The resultant was transferred into a 100 mL Teflon vessel placed inside an autoclave and kept in a hot air oven at 180 °C for 12 h. The product was allowed to

cool naturally, filtered, washed several times with distilled water and ethanol, dried at 120 °C for 6 h and calcined at 500 °C for 2 h in a muffle furnace equipped with a PID temperature controller. The rate of heating was 10 °C min^{-1}.

The synthesized Fe_3O_4-implanted ZnO nanoflakes were deposited with metallic silver by photoreduction. The Fe_3O_4/ZnO nanoflakes (300 mg) were suspended in aqueous methanolic (8% v/v) silver nitrate solution (10 mg in 25 mL) by purging air and were illuminated at 365 nm for 6 h employing eight 8 W mercury lamps. The completion of photodeposition of Ag was confirmed by analytical method. The solid was separated, washed several times with water and ethanol and dried at 120 °C.

2.2. Characterization

The high resolution scanning electron microscopic (HRSEM) images and the energy dispersive X-ray spectrum (EDS) of the sample were recorded under high-vacuum mode using a FEI Quanta FEG 200 high resolution SEM with energy dispersive X-ray (EDX) unit attachment. The synthesized nanomaterial was finely spread on carbon substrate. The high resolution transmission electron microscopic (HRTEM) images and the selected area electron diffractograms (SAED) of the sample were obtained with a Jeol JEM 2100 HRTEM. The nanomaterial was dispersed in ethanol and spread on Formavar coated copper grid for imaging. A Philips CM 200 TEM equipped with Orius CCD camera was also used to obtain SAED at an accelerated voltage of 200 kV. The powder X-ray diffractograms (XRD) were recorded in a 2θ range of 10 to 80° with a PANalytical X'Pert PRO diffractometer using Cu Kα rays of wavelength 0.15406 nm at a tube current of 30 mA at 40 kV. A Renishaw inVia Raman microscope was employed to record the

Raman spectra. The excitation source was an argon laser and the sample was excited at 488 nm. The magnetic measurements were made at room temperature with a Lakeshore 7404 vibrating sample magnetometer (VSM). A CH Instrument electrochemical analyzer 604C was used to record the solid state electrochemical impedance spectra (IS) at room temperature in the frequency range of 0.1 MHz to 1 Hz. While the thickness of the pellets of Fe_3O_4/Ag-deposited ZnO, pristine ZnO and Fe_3O_4 were 1.38, 1.87 and 1.72 mm, respectively, the disc area of all the pellets were 0.5024 cm^2. The UV-visible diffuse reflectance spectra (DRS) were recorded using a Shimadzu UV-2600 spectrophotometer with ISR-2600 integrating sphere attachment. A PerkinElmer LS 55 fluorescence spectrometer was used to record the photoluminescence (PL) spectra at room temperature. The nanomaterials were dispersed in carbon tetrachloride under sonication and the wavelength of excitation was 340 nm. The time-correlated single photon counting (TCSPC) measurements were made with a Horiba Jobin Yuon Fluorolog FL-3-11 spectrofluorimeter. The samples were excited at 295 nm with pulsed Nano-LED.

2.3. Photocatalytic test

The photocatalytic activities were tested employing a photoreactor fitted with four 8 W medium pressure mercury lamps emitting mainly at 365 nm (Sankyo Denki, Japan). To preserve the light intensity, the set of lamps were shielded with a highly polished aluminum reflector. The reaction vessel was a borosilicate glass tube of 15 mm diameter and was placed at the centre of the photoreactor. The fans mounted inside the photoreactor dissipate the generated heat. The photon flux determined by ferrioxalate actinometry was 25.4 μeinstein L^{-1} s^{-1}. Fresh solutions of methylene blue dye were used for the photodegradation experiments. To the dye solution (25

mL), the nanomaterial (25 mg) was added and was purged with air to keep the nanomaterials under suspension and at constant motion. The airflow rate measured by soap bubble method was 7.8 mL s^{-1}. The dissolved oxygen measured with an Elico dissolved oxygen analyzer PE 135 was 9.3 mg L^{-1}. Before illumination, adequate time was provided for the adsorption of the dye to attain equilibrium. At different time of illumination, the nanomaterials were separated and the dye was estimated spectrophotometrically at 662 nm; by measuring the absorbance of the dye at different concentrations (in ppm) a calibration curve was constructed.

2.4. Antibacterial test

Nutrient broth culture of pH 7.4 was obtained by dissolving 13 gm of nutrient broth in 1 L of distilled water and sterilizing the same in an autoclave at 121 °C. MacConkey agar plates were prepared by dissolving 55 g of MacConkey agar in one litre of boiling distilled water, sterilizing the same in an autoclave at 121 °C and pouring into Petri dishes. *E. coli* was inoculated into the nutrient broth and incubated for 24 h at 37 °C. The cultured bacteria were separated at centrifuge (3500 rpm), washed with autoclaved NaCl (0.9%) solution and suspended in NaCl (0.9%) solution. The *E. coli* colony forming units (CFUs) were counted after serial dilution using NaCl (0.9%) solution to get about 150 colonies on the Petri dish. The CFUs were enumerated by a viable count method. The synthesized nanoflakes (25 mg) were added to the bacteria solution (25 mL) and shaken well in the absence of illumination. A known volume of the bacteria solution was removed from the nanomaterial suspension at 0, 5 and 10 min, diluted stepwise and enumerated as described previously.

3. Results and discussion

3.1. Structure

The hydrothermal process yields nanoflakes as seen from the SEM images of the obtained Fe_3O_4-implanted Ag-deposited ZnO. Fig. 1a presents the stacks of the prepared nanoflakes. The obtained nanoflakes are wide and the length and breadth run to several microns. Fig. 1b clearly displays the pores in the synthesized nanoflakes. Fig. 1c presents the EDS of the synthesized nanoflakes. As expected, it displays the presence of silver, zinc, iron and oxygen. The absence of any other element shows the purity of the synthesized nanomaterial. The HRTEM image of the synthesized Ag-deposited nanoflakes is presented in Fig. 2a. It confirms the pores in the synthesized nanoflakes. Fig. 2b shows the Fe_3O_4 core implanted in ZnO lattice deposited with metallic silver. The HRTEM image at high magnification, presented in Fig. 2c, exhibits the lattice fringes of the deposited silver. The observed *d*-spacing of 0.235 nm corresponds to the 111-plane of cubic metallic silver (JCPDS card no. 04-0783). Fig. 2d-f shows the selected area electron diffraction (SAED) patterns of the synthesized nanoflakes obtained at different selected areas and also with two different instruments. The observed concentric rings support the nanocrystallinity of the synthesized material. They index to the planes of hexagonal lattice of ZnO (JCPDS card no. 36-1451). The SAEDs also show the diffraction spots of different planes of cubic Fe_3O_4 (JCPDS card no. 65-3107). This reveals the presence of Fe_3O_4 in the nanoflakes. The diffraction by cubic metallic silver is also observed in the SAEDs of the synthesized nanoflakes (JCPDS card no. 04-0783). This confirms deposition of metallic silver on the obtained nanoflakes.

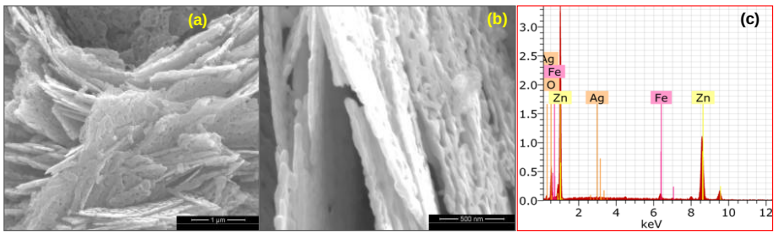

Fig. 1. HRSEM images (a and b) and EDS (c) of Fe_3O_4-implanted Ag-loaded ZnO nanoflakes.

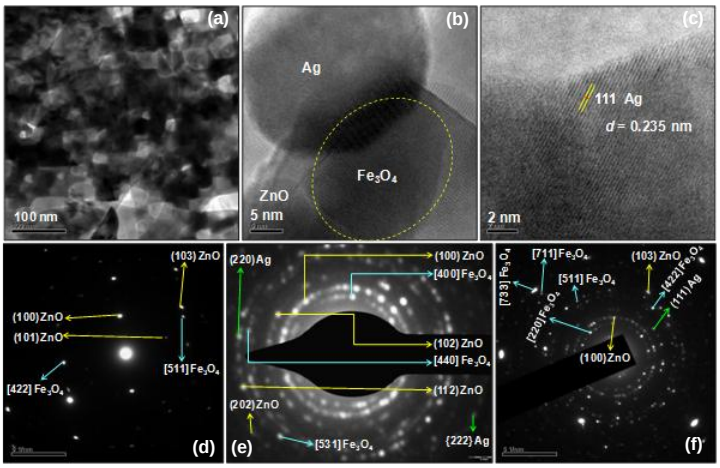

Fig. 2. HRTEM images (a, b, and c) and SAED (d, e, and f) of core/shell Fe_3O_4/Ag-ZnO nanoflakes.

Fig. 3a presents the recorded XRD of the synthesized nanoflakes. The diffractogram agrees with that of hexagonal ZnO. The reference used is JCPDS card no. 36-1451. In addition to the reflections by hexagonal ZnO less intense peaks corresponding to the 111- and 200-planes of cubic silver are observed. This confirms the photodeposition of metallic silver on the hydrothermally synthesized nanocomposite. The percentage of doping of silver, determined by EDS, is 0.3 (at.). It is interesting to note that the recorded XRD does not display the diffraction pattern of cubic Fe_3O_4 (JCPDS card no. 65-3107). This shows the perfect

implantation of Fe_3O_4 core in ZnO lattice. It has been shown that increase of the amount of zinc precursor used for the synthesis decreases the intensity of the XRD peaks of Fe_3O_4 and increases the intensity of diffraction by ZnO.[17,18] Perfect thick ZnO-coating completely suppresses the X-ray reflection by the core Fe_3O_4.[19] The intensity of XRD peak is to rapidly decrease with the increase of the order of diffraction (*n*) and the order of diffraction by the crystal plane of the core is to correspond to the thickness of the shell. Literature survey shows that the Fe_3O_4/ZnO core/shell nanomaterials synthesized by some workers display the XRD patterns of both Fe_3O_4 and ZnO indicating that Fe_3O_4 is either sparsely covered by ZnO layer or the ZnO layer is highly porous.[20-25] Fig. 3a also displays the XRD of precursor Fe_3O_4 nanocrystals used as core. It shows the cubic crystalline structure of Fe_3O_4; the XRD matches with JCPDS card no. 65-3107. The mean crystallite size (*L*) of Fe_3O_4 precursor has been deduced from the full width at half-maximum (fwhm, β) of the most intense peak using Scherrer's formula $L = 0.9\lambda/\beta\cos\theta$, where λ is the wavelength of the X-ray used, θ is the diffraction angle and β is in radian. The deduced mean crystallite size is 33 nm and is in agreement with the size of Fe_3O_4 core observed in the TEM image (Fig. 2b). The Scherrer formula has also been used to deduce the mean size of the silver deposit on the synthesized nanoflakes. The β value of 111-peak of cubic silver observed in the XRD of the synthesized composite nanoflakes has been used for the calculation. The deduced size of the silver deposit is 37 nm. This is in agreement with the size displayed by the TEM image (Fig. 2b).

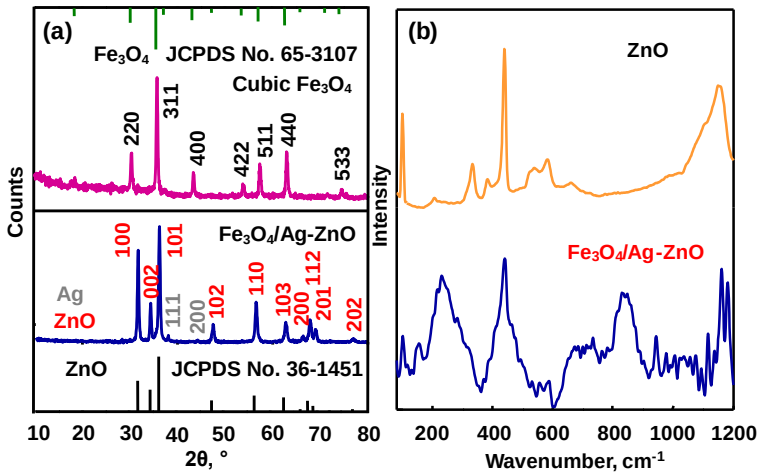

Fig. 3. XRD (a) and Raman spectrum (b) of core/shell Fe_3O_4/Ag-ZnO.

Raman spectroscopy is useful to probe the local structure. Fig. 3b presents the Raman spectrum of the synthesized composite nanoflakes. The intense peak at 440 cm^{-1} and the sharp peak at 101 cm^{-1} are characteristic of the E_2 (high)[19,26-42] and E_2 (low)[19,26,28-31,33,36,37,39,40,42] modes of hexagonal ZnO crystalline structure. The high-frequency E_2 (high) mode involves the vibration of oxygen atoms and the low-frequency E_2 (low) mode is related to the vibration of the zinc sublattice. The intensity of E_2 (high) peak is associated with the crystal quality; stronger is the peak better is the quality. In addition, it is attributed to low intrinsic defects associated with oxygen such as oxygen vacancies (V_o), because it is only associated with the vibration of oxygen atoms.[19] The peak observed at 155 cm^{-1} is in agreement with that of Ag-loaded ZnO prepared by spray pyrolysis technique.[42] It has been assigned to 2TA. Combustion synthesized pristine ZnO also shows a peak at about 150 cm^{-1} but has been assigned to $2E_2$ (low) second-order phonon mode.[37] The strong peak at 230 cm^{-1} corresponds to the local vibration mode (LVM) of Zn-Ag.[26,30-32,39] Multiphonon E_1 (transverse optical, TO) + E_2 (low) scattering mode may correspond to the observed small peak at 530 cm^{-1}.[36,37] This combination mode is

shifted toward higher energy by about 22 cm^{-1} which could possibly be due to the implanted Fe_3O_4 core in the Ag-ZnO nanoflakes. The weak peaks at 556 and 587 cm^{-1} are likely to be due to the A_1 (longitudinal optical, LO)[26,28-31,33,34,36,39,40,42,43] and E_1 (LO) modes,[26-28,30,32,33,35,40,41] respectively. The A_1 (LO) mode is related to the oxygen vacancies and zinc interstitials whereas the E_1 (LO) generally results from impurities and defects. As no impurity was detected by the EDS, structural defects caused by Ag loading is probably a reason for the E_1 (LO) mode. The A_1 (LO) mode indicates the existence of resonance of exciting phonon energy with that of electronic interband transition in the ZnO lattice.[29] It occurs widely at 574 ± 5 cm^{-1} but that of the synthesized core/shell Fe_3O_4/Ag-deposited ZnO is lower in energy by about 18 cm^{-1} which is probably due to implantation of Fe_3O_4 core in Ag-loaded ZnO nanoflakes. The broad peak observed around 670 cm^{-1} is similar to that of hydrothermally synthesized Ag-loaded ZnO nanostructures[27] and is attributed to TA + LO combination modes with A_1 symmetry.[42] The Raman peak appearing at 733 cm^{-1} is attributed to $2A_1$ (TO) second-order polar mode.[36] This mode is about 20 cm^{-1} lower in energy compared to the Ag-deposited ZnO synthesized by Zeferino *et al.*,[36] and the possible reason could be the implanted Fe_3O_4 core. The intense band at around 830 cm^{-1} may be assigned to the LA + LO combination with A_1 symmetry.[42] The sharp peak at 943 cm^{-1} is likely due to 2TO overtone.[42] The strong peak at 1161 cm^{-1} and the less intense one at 1116 cm^{-1} can be resolved to second-order $2E_1$ (LO) and $2A_1$ (LO) phonons, respectively.[29,42] The sharp peak at 1182 cm^{-1} is likely to represent the acoustic combination of A_1 and E_2 modes.[37] Fig. 3b also presents the Raman spectrum of hydrothermally synthesized pristine ZnO nanoflakes. The E_2 (low), E_2 (high), A_1 (TO), A_1 (LO), E_1 (LO), 2TA (M), E_2 (high)

– E_2 (low), $2E_2$ (M) + A_1 (LO) and 2 LO Raman modes are observed at 100, 438, 380, 535, 579, 207, 330, 666 and 1180 cm^{-1}, respectively. Examination of the intensities of the E_2 (high) modes of Fe_3O_4/Ag-loaded ZnO and pristine ZnO reveals that implantation of Fe_3O_4 core in ZnO and loading the same with silver lowers the crystallinity. The appearance of 2TA/$2E_2$ (low) second-order phonon mode/s in the core/shell sample indicates the existence of oxygen vacancies in the synthesized nanocomposite. The appearance of intense LVM at 230 cm^{-1} confirms the Ag-deposition. Further, the Raman spectra show suppression of the second-order modes of ZnO on implantation of Fe_3O_4 in ZnO nanoflakes and loading ZnO with Ag.

3.2. Magnetic properties

The magnetic hysteresis loops of the synthesized Ag-loaded core/shell nanoflakes and the precursor Fe_3O_4 nanocrystals, obtained at room temperature, are presented in Fig. 4a. The hysteresis loops are of normal S-shape. The coercivities (H_C) of the nanomaterials are inferred from the "thickness" of the loops. The H_C of core/shell Fe_3O_4/Ag-deposited ZnO nanoflakes and precursor Fe_3O_4 nanocrystals are 482 and 35 Oe, respectively. Encapsulation of Fe_3O_4 nanocrystals by Ag-loaded ZnO increases the coercivity. The H_C of precursor Fe_3O_4 nanocrystals is almost the same that of Fe_3O_4 microspheres (37 Oe)[44] but is less than those of Fe_3O_4 microoctahedra (103 Oe) prepared by hydrothermal reduction of $K_3[Fe(CN)_6]$[45] and hydrothermally obtained Fe_3O_4 octahedra (74 Oe).[46] The remanent magnetization (M_R) of the synthesized composite nanoflakes and precursor Fe_3O_4 nanocrystals are 0.16 and 0.1 emu g^{-1}, respectively. The determined M_R values are much smaller than those of hydrothermally prepared Fe_3O_4 octahedra (4.2 emu g^{-1})[46] and Fe_3O_4

microoctahedra (13.5 emu g^{-1}) derived by hydrothermal reduction of $K_3[Fe(CN)_6]$. [45] The insignificant M_R values of Fe_3O_4/Ag-deposited ZnO core/shell nanosheets and precursor Fe_3O_4 nanoparticles suggest superparamagnetic character of the synthesized composite core/shell nanoflakes and precursor Fe_3O_4 nanocrystals. The saturation magnetization (M_S) of the synthesized photocatalytic nanoflakes and precursor Fe_3O_4 nanoparticles, respectively, are 0.49 and 1.6 emu g^{-1}. The M_S value of Fe_3O_4-implanted Ag-deposited ZnO nanoflakes is much less than that of precursor Fe_3O_4 nanocrystals and the possible reason is that Fe_3O_4 nanocrystals are deeply buried in Ag-loaded ZnO nanoflakes. Experiment with a tiny magnet shows that all the nanoparticles are attracted by the magnet which reveals that the iron oxide core is present in all the nanocrystals.

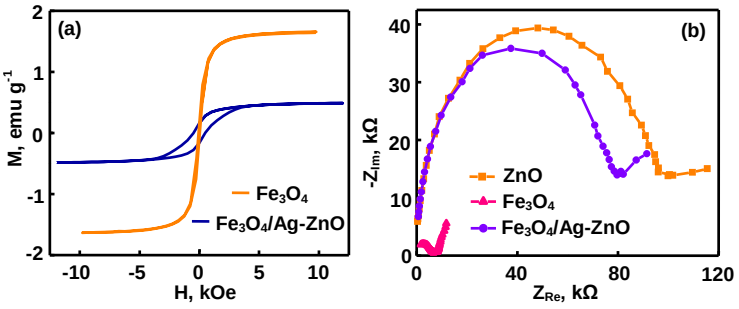

Fig. 4. The M – H curves (a) and the Nyquist plots (b).

3.3. Electrical properties

Charge carrier transfer plays a significant role in semiconductor-photocatalysis. The photogenerated charge carriers are to migrate to the crystal surface to react with the adsorbed species to bring in photocatalysis. Solid state electrochemical impedance spectroscopy is a versatile technique to probe the electrical properties of semiconductor nanomaterials. Impedance measurement in the frequency range 0.1 MHz - 1 Hz shows decrease of impedance with increase of frequency revealing the

capacitance of the nanomaterials examined. A popular format of analyzing the impedance data is through the Nyquist plot. The complex solid state impedance spectra of core/shell Fe_3O_4/Ag-ZnO nanoflakes, precursor Fe_3O_4 nanoparticles and pristine ZnO nanoflakes are presented in Fig. 4b. Intragranular (bulk) resistance and intergranular (grain boundary) resistance contribute to the overall crystal resistance. The intragranular resistance corresponds to polarization or charge-transfer resistance (R_{CT}). The R_{CT} is related to the Warburg resistance which is the resistance to mass transfer and is controlled by the specific conductance (σ). The intergranular resistance refers to ohmic (R_{Ω}) or uncompensated resistance. The constant phase element is related to non-uniform distribution of current due to material heterogeneity and is equivalent to double layer capacitance (C). The determined (i) R_{Ω}, (ii) R_{CT}, (iii) σ and (iv) C values of the synthesized core/shell Fe_3O_4/Ag-deposited ZnO nanoflakes, ZnO nanoflakes and precursor Fe_3O_4 nanoparticles are (i) 0.68, 0.38 and 1.7 kΩ, (ii) 79, 100 and 5 kΩ, (iii) 0.44, 0.37 and 6.7 mS m^{-1} and (iv) 0.53, 0.29 and 0.57 nF, respectively. The R_{Ω}, R_{CT}, σ and C values of the synthesized core/shell nanoflakes lie between those of ZnO nanoflakes and Fe_3O_4 nanocrystals. A possible reason is that both Fe_3O_4 and ZnO are the constituents of the synthesized core/shell nanocomposite.

3.4. Optical properties

Fig. 5a displays the UV visible DRS of core/shell Fe_3O_4/Ag-ZnO nanoflakes and that of precursor Fe_3O_4 nanocrystals. The DRS are presented in terms of $F(R)$, deduced from the measured reflectance (R) by the application of the Kubelka-Munk (K-M) algorithm, $F(R) = (1 - R)^2/2R$. The absorption edge of the synthesized core/shell Fe_3O_4/Ag-ZnO nanosheets is 391 nm which corresponds to band gap

energy of 3.17 eV. This band gap energy is in agreement with that of pristine ZnO and confirms the ZnO shell in the synthesized core/shell nanomaterial. The synthesized core/shell Fe_3O_4/Ag-ZnO nanoflakes also significantly absorb visible light and this is due to the Fe_3O_4 core. The DRS of precursor Fe_3O_4 exhibits its strong visible light absorption.

Fig. 5b presents the photoluminescence spectra of core/shell Fe_3O_4/Ag-ZnO and pristine ZnO nanoflakes. The spectra were recorded at room temperature. Both the samples show near band gap emission (NBE) and deep level emission (DLE). Furthermore, both the spectra are similar. The NBE is due to radiative recombination of photogenerated free electron-hole pairs. The DLE arises because of the different intrinsic and extrinsic structural defects. Both the nanomaterials show violet emission at 420 nm, blue emission at 457 nm and blue-green emission at 481 nm. These emissions are assigned to band-edge free excitons and bound excitations.[47,48] The blue emission is due to electron transition from the shallow donor level of oxygen vacancies to valence band (VB) and electron transition from shallow donor level of zinc interstitials to the VB.[48] The weak green emission at 526 nm is related to oxygen vacancies and other vacancy-related defects.[49] This emission energy corresponds to the electron transition from deep-level donor of the ionized oxygen vacancies to the VB. Yellow emission is attributed to excess oxygen and absence of such emission shows absence of excess oxygen in the synthesized samples.[49]

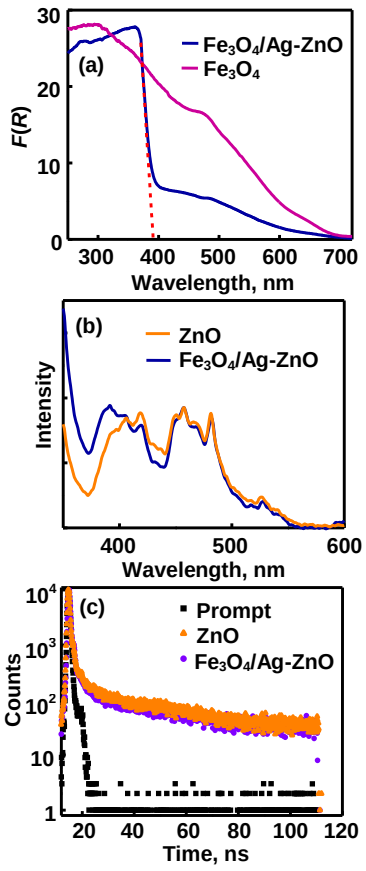

Fig. 5. UV-vis. diffuse reflectance (a), PL (b) and TRPL (c) spectra of Fe_3O_4/Ag-ZnO.

Time-resolved photoluminescence (TRPL) spectroscopy is a powerful tool to study the optical properties of nanocrystalline semiconductors. The lifetime of exciton can be obtained by TRPL spectroscopy. The lifetimes of the photoexcited state of core/shell Fe_3O_4/Ag-ZnO and pristine ZnO nanoflakes were studied by time-correlated single photon counting (TCSPC) lifetime spectroscopy. The NBE of both the nanomaterials is at ~390 nm and the TRPL traces were followed at 395 nm. This wavelength corresponds to free exciton band. The fluorescence decay curves are displayed in Fig. 5c. The nanomaterials were excited at 295 nm. The overlap of both the curves confirms the presence of ZnO shell in the synthesized

core/shell nanoflakes. The energy of excitation (4.20 eV) is far larger than the band gap energy of the synthesized nanomaterials and the excitation first undergoes thermalization to form an excitation. The excitation further relaxes prior to radiation. At room temperature, these radiation processes reach completion in picosecond-timescale.[50] Both the decay data fit satisfactorily to a triexponential decay curve, $F(t) = a_1 \exp(-t/\tau_1) + a_2 \exp(-t/\tau_2) + a_3 \exp(-t/\tau_3)$, where a_1, a_2 and a_3 are preexponentials associated with the concentration of emitting species 1, 2 and 3, τ_1, τ_2 and τ_3 are the corresponding lifetimes, t is the time of measurement and $F(t)$ is the photon counts at time t. The triexponential kinetic decay reveals that the emission involves three different decay processes. However, the exact mechanism is not yet explored. The deduced lifetimes of the three emission processes of excited (i) core/shell Fe_3O_4/Ag-ZnO and (ii) pristine ZnO nanosheets are (i) 6 ps, 1.6 ns and 25 ns and (ii) 81 ps, 2.1 ns and 28 ns, respectively. The relative amplitudes of the fast, medium and long decays of (i) Fe_3O_4/Ag-ZnO (ii) ZnO are (i) 1.00, ~0.00 and ~0.00 and (ii) 0.995, 0.004 and 0.0005, respectively. In both the cases, the fast decay is the predominant event. The fast decay which takes place in picosecond-time scale is likely to represent the recombination of free excitions in ZnO; Jung *et al*.,[50] report the lifetime of free excitons in ZnO films as 180 ps. The obtained medium decay time is in agreement with those reported by Jung *et al*., (1 ns)[50] and Layek et al (1.5-2.8 ns).[51] The obtained long decay time is in accordance with the earlier report (14-26 ns).[51] The medium and long decays are attributed to recombination of trapped charge carriers and Layek et al.,[51] has assigned τ_2 to radiative recombination of shallowly trapped electrons and deep trapped holes. Examination of the obtained lifetimes of core/shell Fe_3O_4/Ag-ZnO and pristine ZnO

reveals that the presence of Fe_3O_4 core in ZnO nullifies the effect of Ag on ZnO. Nanodeposits of silver on the surface of ZnO can act as electron-hole separation centers.[41,52] The Fermi level of silver is lower than the conduction band (CB) energy level of ZnO and hence migration of the photogenerated electron from CB of ZnO to the Fermi level of Ag is thermodynamically feasible (Fig. 6). This electron transfer from ZnO to Ag is likely to enhance the lifetime of charge carriers. On the other hand, the CB edge of ZnO is more cathodic than that of core Fe_3O_4. Similarly, the VB edge of ZnO is more anodic than that of Fe_3O_4 core. This allows migration of photoformed charge carriers from the ZnO shell to the Fe_3O_4 core, where they get quenched. Fe_3O_4 core is completely covered by the ZnO shell and the charge carriers are confined to the Fe_3O_4 core. That is, Fe_3O_4 core promotes charge carrier quenching and Ag nanodeposit on ZnO surface favors charge separation. As these two processes operate oppositely the lifetime of excited core/shell Fe_3O_4/Ag-ZnO is not significantly different from that of pristine ZnO.

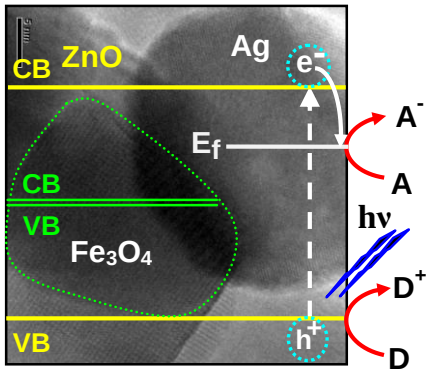

Fig. 6. The CB and VB edges.

3.5. Photocatalytic activity

The spectral time scan of degradation of methylene blue dye catalyzed by core/shell Fe_3O_4/Ag-ZnO nanoflakes under UV A light is presented in Fig. 7a. The time

profile of the degradation of dye is displayed in Fig. 7b. For the purpose of comparison, the corresponding curve with Fe_3O_4 nanocrystals as photocatalyst and that of photolysis are presented. The observed dye degradation profiles demonstrate the photocatalytic activity of the synthesized core/shell Fe_3O_4/Ag-ZnO nanoflakes. Furthermore, the synthesized composite core/shell nanoflakes are reusable photocatalyst. Fig. 7c shows that the photocatalytic activity is not lost on repeated usage. In addition, the synthesized composite nanosheets are photostable. Estimation of Zn^{2+} in the reaction solution before and after photodegradation of the dye by atomic absorption spectroscopy shows the absence of release of Zn^{2+} during photocatalysis under the experimental conditions.

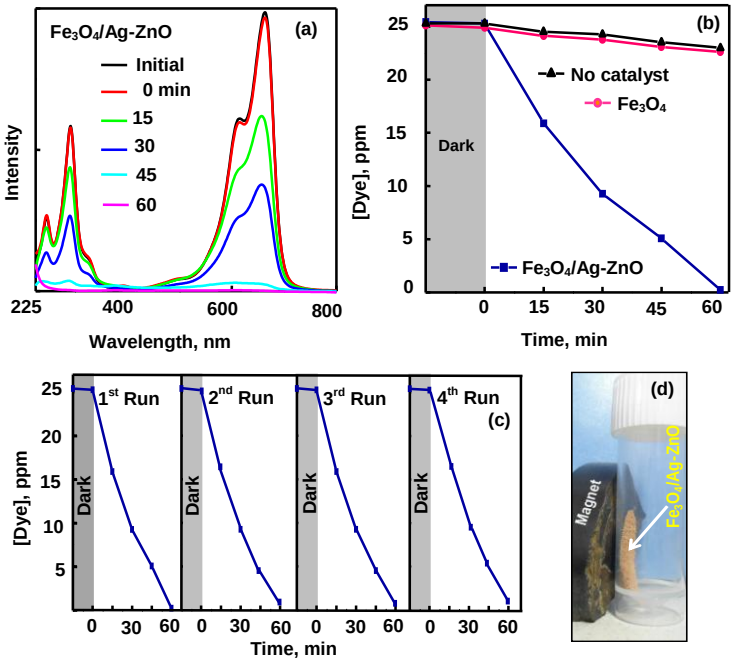

Fig. 7. Spectral time scan (a) and time profile (b) of dye degradation and reusability (c) and attraction by magnet (d) of the photocatalyst.

3.6. Magnetic recovery

Recovery of the photocatalyst nanomaterial is the stumbling block for adoption of this emerging technology by industries. Magnetic separation is possible in the case

of photocatalyst nanomaterial with magnetic core. Fig. 7d shows that the synthesized Fe_3O_4-implanted Ag-deposited ZnO nanoflakes are attracted by magnet enabling magnetic recovery of the photocatalytic nanomaterial.

3.7. Bacteria disinfection

Fig. 8 presents the population of *E. coli*, counted in terms of CFU, in the presence of core/shell Fe_3O_4/Ag-ZnO nanoflakes at 0, 5 and 10 min. The bacteria disinfection by the suspended synthesized composite nanoflakes was investigated in the absence of direct illumination. In the absence of the synthesized composite nanoflakes the *E. coli* population remained intact during the experimental period. The observed results demonstrate the antibacterial activity of Fe_3O_4/Ag-ZnO nanoflakes. Fig. 8 also displays a pair of photographs showing the *E. coli* population at the start of mixing the core/shell composite nanosheets with the bacteria solution and at 10 min. Both ZnO and Ag nanoparticles are well known bactericides and hence are the Ag-loaded ZnO nanomaterial. The mechanisms of bacteria-disinfection by Ag nanoparticles[9] and by nanocrystalline ZnO [8] are well known and that by Ag-loaded ZnO nanomaterials is unlikely to be different.[10]

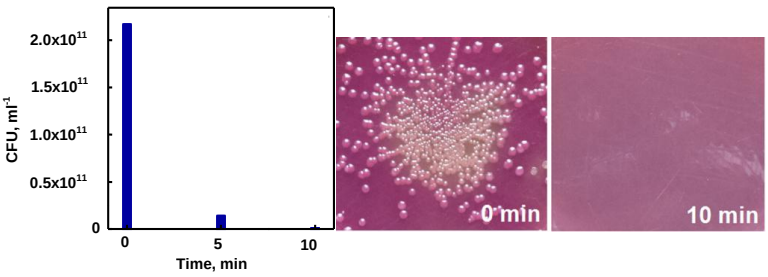

Fig. 8. *E. coli* disinfection by Fe_3O_4-implanted Ag-loaded ZnO nanoflakes.

4. Conclusions

Fe_3O_4-Implanted Ag-loaded ZnO nanoflakes were synthesized by hydrothermal treatment followed by photodeposition. The synthesized nanoflakes

have been characterized by X-ray and selected area electron diffractometry, high resolution scanning electron and transmission electron microscopies, vibrating sample magnetometry and energy dispersive X-ray, Raman, solid state electrochemical impedance, UV-visible diffuse reflectance, photoluminescence and time correlated single photon counting lifetime spectroscopies. The efficient photocatalytic and antibacterial activities of the synthesized core/shell composite nanoflakes have been demonstrated through dye-degradation and *E. coli*-inactivation. The recovery of the core/shell nanoflakes using a tiny magnet has been shown.

Acknowledgements

The financial support for the research (SR/S1/PC-41/2011) by the Science and Engineering Research Board (SERB), Department of Science and Technology (DST), New Delhi is gratefully acknowledged. Further, Prof. C. Karunakaran thanks the Council and Scientific and Industrial Research (CSIR), New Delhi, for the Emeritus Scientist Scheme 21(0887)/12/EMR-II. P. Vinayagamoorthy is grateful to DST for the fellowship.

References

1 Y. Li, W. Xie, X. Hu, G. Shen, X. Zhou, Y. Xiang, X. Zhao and P. Fang, *Langmuir*, 2010, **26**, 591-597.

2 W.L. Ong, S. Natarajan, B. Kloostra and G.W. Ho, *Nanoscale*, 2013, **5**, 5568-5575.

3 D. Zhang, J. Li, Y. Chen, Q.-S. Wu and Y.-P. Ding, *CrysEngCommun.*, 2012, **14**, 6738-6743.

4 H.R. Liu, G.X. Shao, J.F. Zhao, Z.X. Zhang, Y. Zhang, J. Liang, X.G. Liu, H.S. Jia and B.S. Xu, *J. Phys. Chem. C*, 2012, **116**, 16182-16190.

5 M.E. Aguirre, H.B. Rodriguez, E.S. Roman, A. Feldhoff and M.A. Grela, *J. Phys. Chem. C*, 2011, **115**, 24967-24974.

6 Y. Zheng, L. Zheng, Y. Zhan, X. Li, Q. Zheng and K. Wei, *Inorg. Chem.*, 2007, 4**6**, 6980-6986.

7 Y. Zheng, C. Chen, Y. Zhan, X. Lin, Q. Zheng, K. Wei and J. Zhu, *J. Phys. Chem. C*, 2008, **112**, 10773-10777.

8 K. R. Raghupathi, T. Koodali and A. C. Manna, *Langmuir*, 2011, **27**, 4020-4028.

9 V. K. Sharma, R. A. Yngard and Y. Lin, *Adv. Colloid Interface Sci*., 2009, **145**, 83-96.

10 S. Ghosh, V.S. Goudar, K.G. Padmalekha, S.V. Bhat, S.S. Indi, H.N. Vasan, *RSC. Adv*., 2012, **2**, 930-940.

11 C. Karunakaran, V. Rajeswari and P. Gomathisankar, *Syn. React. Inorg. Me.*, 2011, **41**, 369-375.

12 C. Karunakaran, V. Rajeswari and P. Gomathisankar, *Mater. Sci. Semicond. Process.*, 2011, **14**, 133-138.

13 C. Karunakaran, V. Rajeswari and P. Gomathisankar, *Solid State Sci.*, 2011, **13**, 923-928.

14 C. Karunakaran, V. Rajeswari and P. Gomathisankar, *Superlattices Microstruct.*, 2011, **50**, 234-241.

15 S. Shylesh, V. Schunemann and W. R. Thiel, *Angew. Chem. Int. Ed*., 2010, **49**, 3428-3459.

16 X. Feng, H. Guo, K. Patel, H. Zhou, X. Lou, *Chem. Eng. J*., 2014, **244**, 327-334.

17 H. Liu, J. Wu, J. H. Min, X. Zhang and Y.K. Kim, *Mater. Res. Bull*., 2013, **48**, 551-558.

18 A. A. Shal and A. Jafari, *J. Supercond. Nov. Magn*., 2014, **27**, 1531-1538.

19 C. Karunakaran, P. Vinayagamoorthy and J. Jayabharathi, *Langmuir*, 2014, **30**, 15031-15039.

20 S. Ghasemi, M. Heidary, M.A. Faramarzi and Z. Habibi, *J. Mol. Catal. B*, 2014, **100**, 121-128.

21 W. Chiu, P. Khiew, M. Cloke, D. Isa, H. Lim, T. Tan, N. Huang, S. Radiman, R. Abd-Shukor, M.A. Abd. Hamid and C. Chia, *J. Phys. Chem. C*, 2010, **114**, 8212-8218.

22 J. Wan, H. Li and K. Chen, *Mater. Chem. Phys*., 2009, **114**, 30-32.

23 R.Y. Hong, S.Z. Zhang, G.Q. Di, H.Z. Li, Y. Zheng, J. Ding and D.G. Wei, *Mater. Res. Bull.*, 2008, **43**, 2457-2468.

24 Y.-J. Chen, F. Zhang, G.-g. Zhao, X.-y. Fang, H.-B. Jin, P. Gao, C.-L. Zhu, M.-S. Cao and G. Xiao, *J. Phys. Chem. C*, 2010, **114**, 9239-9244.

25 S. Singh, K.C. Barick and D. Bahadur, *J. Mater. Chem. A*, 2013, **1**, 3325-3333.

26 H.Q. Bian, S.Y. Ma, Z.M. Zhang, J.M. Gao and H.B. Zhu, *J. Cryst. Growth*, 2014, **394**, 132-136.

27 X.-Y. Ye, Y.-M. Zhou, Y.-Q. Sun, J. Chen and Z.-Q. Wang, *J. Nanopart. Res*., 2009, **11**, 1159-1166.

28 L.N. Wang, L.Z. Hu, H.Q. Zhang, Y. Qiu, Y. Lang, G.Q. Liu, J.Y. Ji, J.X. Ma and Z.W. Zhao, *Mater. Sci. Semicond. Process*., 2011, **14**, 274-277.

29 S.S. Shinde, C.H. Bhosale and K.Y. Rajpure, *Spectrochim. Acta A*, 2012, **98**, 453-456.

30 H.Q. Bian, S.Y. Ma, F.M. Li and H.B. Zhu, *Superlattices Microstruct*., 2013, **58**, 171-177.

31 W.J. Li, C.Y. Kong, H.B. Ruan, G.P. Qin, G.J. Huang, T.Y. Yang, W.W. Liang, Y.H. Zhao, X.D. Meng, P. Yu, Y.T. Cui and L. Fang, *Solid State Commun*., 2012, **152**, 147-150.

32 G. Zhu, Y. Liu, H. Xu, Y. Chen, X. Shen and Z. Xu, *CrystEngComm*, 2012, **14**, 719-725.

33 L.-N. Wang, L.-Z. Hu, H.-Q. Zhang, Y. Qiu, Y. Lang, G.-Q. Liu, G.-W. Qu, J.-Y. Ji and J.-X. Ma, *Chin. Phys. Lett*., 2012, **29**, 017302.

34 C. Chen, Y. Zheng, Y. Zhan, X. Lin, Q. Zheng and K. Wei, *Dalton Trans*., 2011, **40**, 9566-9570.

35 T. Jan, J. Iqbal, M. Ismail and A. Mahood, *J. Appl. Phys*., 2014, **115**, 154308.

36 R. S. Zeferino, M.B. Flores and U. Pal, *J. Appl. Phys*., 2011, **109**, 014308.

37 S. Saravanan, M. Silambarasan and T. Soga, *Jpn. J. Appl. Phys*., 2014, **53**, 11RF01.

38 B.S. Reddy, S.V. Reddy and N.K. Reddy, *J. Mater. Sci: Mater. Electron*., 2013, **24**, 5204-5210.

39 X.B. Wang, C. Song, K.W. Geng, F. Zeng and F. Pan, *J. Phys. D*, 2006, **39**, 4992-4996.

40 O. Lupan, L. Chow, L.K. Ono, B.R. Cuenya, G. Chal, H. Khallaf, S. Park and A. Schulte, *J. Phys. Chem. C*, 2010, **114**, 12401-12408.

41 R. Georgekutty, M.K. Seery and S.C. Pillai, *J. Phys. Chem. C*, 2008, **112**, 13563-13570.

42 S.S. Shinde, C.H. Bhosale and K.Y. Rajpure, *J. Photochem. Photobiol. B*, 2012, **117**, 262-268.

43 J. Yin, Y. Zang, C. Yue, Z. Wu, S. Wu, J. Li and Z. Wu, *J. Mater. Chem*., 2012, **22**, 7902-7909.

44 W.-W. Wang and J.-L. Yao, *Mater. Res. Bull*., 2010, **45**, 710-716.

45 J. Zhang, Q. Kong, J. Du, D. Ma, G. Xi and Y. Qian, *J. Cryst. Growth*, 2007, **308**, 159-169.

46 C. Hu, Z. Gao and X. Yang, *Chem. Phys. Lett.*, 2006, **429**, 513-517.

47 J. Becker, K.R. Raghupathi, St. J. Pierre, D. Zhao and R.T. Koodali, *J. Phys. Chem. C*, 2011, **115**, 13844-13850.

48 L. Jing, Y. Qu, B. Wang, S. Li, B. Jiang, L. Yang, W. Fu, H. Fu and J. Sun, *Sol. Energy Mater. Sol. Cells*, 2006, **90**, 1773-1787.

49 X. Wang, Q. Zhang, Q. Wan, G. Dai, C. Zhou and B. Zou, *J. Phys. Chem. C*, 2011, **115**, 2769-1775.

50 S.W. Jung, W.L. Park, H.D. Cheong, G.-C. Yi and H.M. Jang, *Appl. Phys. Lett.*, 2002, **80**, 1924-1926.

51 A. Layek, B. Manna and A. Chowdhury, *Chem. Phys. Lett.*, 2012, **539-540**, 133-138.

52 C. Karunakaran, P. Anilkumar and P. Gomathisankar, *Monatsh. Chem.*, 2010, **141**, 529-537.

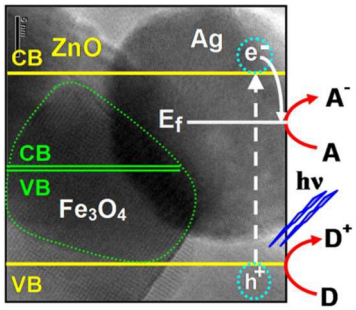

Tri-functional Ag-loaded ZnO nanoflakes with Fe_3O_4 core synthesized by hydrothermal method followed by photodeposition